2010 IEEE International Conference on Robotics and Automation
Anchorage Convention District
May 3-8, 2010, Anchorage, Alaska, USA

A Compliant Constant-Force Mechanism for Adaptive Robot End-Effector Operations

Chao-Chieh Lan, *Member*, IEEE, Jhe-Hong Wang, Yi-Ho Chen

***Abstract*—Force regulation is a challenging issue of robot end-effectors when interacting with unknown environments. It often requires sophisticated sensors with computerized control. This paper presents a constant-force mechanism (CFM) to regulate the contact force of a robot end-effector. The proposed CFM is a monolithic compliant mechanism that has no frictional wear and is capable of miniaturization. Due to the passive mechanism, additional sensors and control effort are minimized. We propose a design formulation to find the optimal CFM shape that produces the most constant force. The reaction force to input displacement curve is invariant of size and flexural rigidity. The curve can be manipulated depending on the desirable situations. The CFM is validated through an experiment. When equipped with the CFM, an illustrative end-effector can adapt to a surface of variable height, without additional motion programming. With the merits shown, we expect this type of elastic mechanism can be utilized in robot end-effectors to provide friendly contact with environment.**

***Index Terms*—Constant-force mechanism, zero stiffness, robot end-effector, force regulation, compliant mechanism, shape design.**

I. Introduction

A constant-force mechanism (CFM) provides a nearly constant output force over a range of input displacements. Unlike helical springs and other elastic structures, a CFM does not obey Hooke's law. It is useful when an unknown deflection is applied to a system the reaction force of which must be a specified constant regardless of deflection. As the force is kept invariable without additional sensors and actuators, the use of a CFM reduces control effort, increases reliability, and is insensitive to mating/assembly imperfections. Ready examples are the constant-force and constant-torque springs that made of one or more rolled strips of spring steel [1]. They are widely used for wire retrieving, weight counterbalancing, and length adjusting.

Although a constant force can be generated by using active (see Ref. [2] for a pneumatic example) devices, CFMs are usually made of passive elastic elements to reduce complexity introduced by extra power input. The simplest CFM makes use of the buckling of elastic structures. See Fig. 1(a) for an example. Sönmez [3] introduced a compliant force dwell mechanism using buckling beams and arcs. Besides buckling, most other CFMs take advantage of the integration of positive and negative stiffness mechanisms; see Fig. 1(b) for an example. Using this principle, standard linkages can be converted to CFMs by embedding torsional springs and/or linear springs [4−5]. Boyle *et al*. [6] further proposed a constant-force compression mechanism by using leaf springs. Nahar and Sugar [7] implemented a constant-force double-slider mechanism. The force magnitude of the mechanism can be adjusted by changing its spring length. To be miniaturizable, CFM's made of one piece of material are more favorable. Pedersen *et al*. [8] designed a monolithic compliant mechanism that delivers a constant output force.

Since the derivative of a constant force is zero, CFMs are also termed zero-stiffness or quasi-zero stiffness mechanisms. They have been used in vibration protecting [9] and energy absorption [10] systems. To explore more applications, Meaders and Mattson [11] optimized the shape of a constant-force spring for robust electrical contact. Howell *et al.* [12] designed a constant-force exercise machine. A constant-force rail clamp is found in [13]. Despite the numerous applications, the merits of CFMs in robotics have not been fully explored. Force regulation is essential for robot end-effectors operating in an unknown environment. They include peg-in-the-hole operation, deburring, painting, grinding, polishing, and interacting with natural objects. To prevent damage caused by excessive contact force between end-effector and environment, it is necessary to maintain a constant contact force while following an unknown trajectory. A force sensor is usually inserted between the robot arm and end-effector to feedback force signal, in order to control the impedance of the end-effector. As illustrated in Fig. 1(c), an end-effector moves through a surface with variable heights. To prevent jam and bind, a controller with force sensor feedback is required to move the end-effector left and right to adapt to the surface and maintain a constant force. Advanced control algorithms [14−15] have been developed to precisely control the contact force under unknown environments. When the end-effector is attached to a CFM shown in Fig. 1(d), the end-effector tip can retreat to fit the surface height without yielding excessive contact force. Although the force cannot be made extremely constant due to the nature of CFMs, the elimination of force sensors and controllers makes CFMs a very reliable alternative when end-effectors face an unknown environment with limited surface variation.

This paper aims to develop a compliant CFM that is suitable for end-effector force regulation. Compared with CFMs the manipulation of which relies on turning pairs and cam pairs, the proposed one-piece CFM is wear-free, scalable, and requires minimum assembly. This CFM is to be placed between an end-effector and robot arm for force regulation under unknown environments. In what follows, an optimization formulation is presented to design the shape of the CFM; the aim is to create a displacement range that has reaction force as constant as possible. A CFM prototype is fabricated and validated experimentally. Finally, the CFM is installed in an emulating end-effector to illustrate its force adaptivity.

This work was supported in part by the Ministry of Education, Taiwan, R.O.C. under the NCKU Project of Promoting Academic Excellence and Developing World Class Research Centers.

C.-C. Lan, J.-H. Wang, and Y.-H. Chen are with the Department of Mechanical Engineering, National Cheng Kung University, No. 1, University Rd., Tainan, Taiwan. (corresponding author e-mail: cclan@mail.ncku.edu.tw).

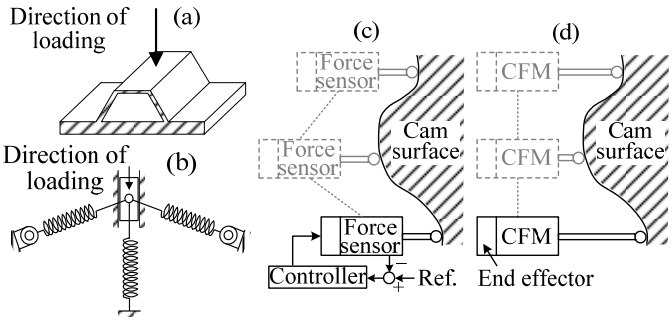

Fig. 1 (a) Buckle type CFM (b) A CFM with three springs
(c) End-effector with an active force controller
(d) End-effector with a passive CFM

II. Design Formulation of a Constant-Force Mechanism

Fig. 2(a) shows the reaction force to displacement (F–Δ) curve of a spring and Fig. 2(b) of a CFM. A typical spring (and most other types of material) produces an output force the magnitude of which is proportional to the input displacement (Hooke's law). A CFM, on the other hand, generates a nearly constant output force over a range of input displacements. Ideally, the constant-force range should be flat as indicated by the solid line. However, actual elastic mechanisms do not fully follow the ideal F–Δ curve. There will be maximal and minimal peaks that make the curve fluctuate. This is similar to the structural snap-through buckling behavior, except the goal here is to reduce to gap between the peaks. To define a reasonable constant-force (operational) range, we first characterize the F–Δ curve of a typical CFM in Fig. 2(c). Given an input displacement $\Delta=d$, the maximal reaction force should occur at d and it is denoted as the nominal constant force F_d. Within the displacement range where the allowable stress of the beams is not violated, the lower limit of the operational range is defined at $\Delta=c$, where $F(c) = 0.95\times F_d$. Hence the operational range is defined between c and d.

As CFMs have a F–Δ curve that is drastically different from other elastic structures, their configuration requires a delicate design. Without loss of generality, we consider a CFM shown in Fig. 3. The concept of this CFM is derived from that in Fig. 1(b), except that coil springs are replaced by homogenous slender beams. The CFM consists of two symmetric parts separated by a distance δ. The input displacement is given on the top rigid block along the negative y direction and the CFM generates a reaction force F in the positive y direction. Taking advantage of symmetry, we only consider the right hand part of the CFM, which consists

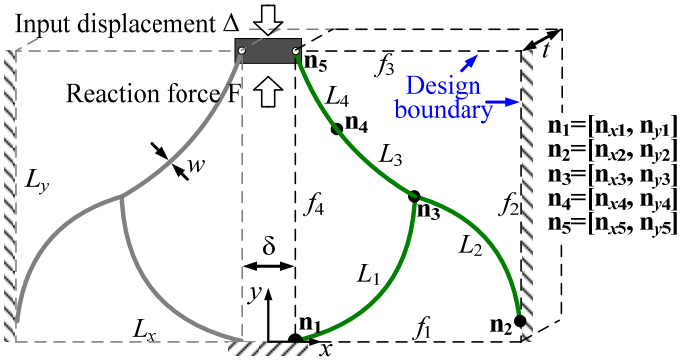

Fig. 3 Schematic of the CFM

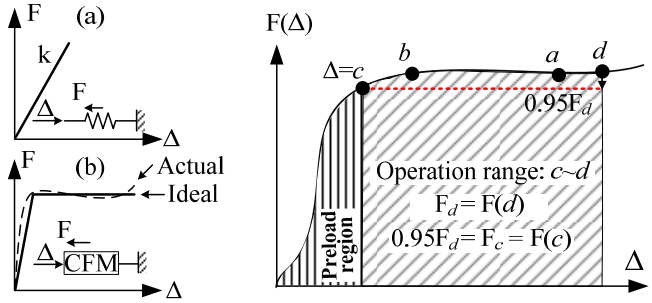

Fig. 2 (a) F–Δ curve of a spring (b) F–Δ curve of a CFM
(c) Characterization of the F–Δ curve

of four beams (with length L_1 to L_4) enclosed in a rectangular design boundary (f_1–f_4). The beams are mathematically separated by five nodes ($\mathbf{n}_1$ to $\mathbf{n}_5$), where beam angles at $\mathbf{n}_3$ and $\mathbf{n}_4$ are not necessarily continuous. Due to symmetry, node $\mathbf{n}_5$ can be considered as a slider which is located on boundary f_4. To find a CFM shape that has a nearly constant F, we formulate an optimization problem with an objective function that depends on the reaction forces at two pre-specified displacements $\Delta=a$ and $\Delta=b$ (a > b).

$$\text{Objective:} \qquad \min\,[F(a)/F(b) - 1] \tag{1}$$

Eq. (1) aims to match the values of $F(a)$ and $F(b)$ such that the objective function is close to zero. To make the segment between c and d is as flat as possible, the values of a and b are evenly chosen between 0 and d. They may be smaller or larger than c depending on the mechanism configuration. Note that the F–Δ curve is generally increasing and hence F(a) > F(b). Apparently the beam shapes and node positions are the primarily design variables for the objective.

2.1 Parameterization of CFM shape

Each beam in Fig. 3 has a rectangular cross-section with in-plane thickness w and out-of-plane thickness t. The flexural rigidity of the beams is denoted as EI where E is the elastic modulus and $I= tw^3/12$ is the second moment of area. Fig. 4 shows the beam model. The un-deflected beam is described by a shape (intrinsic) function $\eta(u)$, where $u \in [0\ 1]$ is a non-dimensional arc length along its neutral axis and η measures the angle of rotation (or slope, in radians) along u. Upon external load, the deflected beam is characterized by another function $\psi(u)$. The beam reaction moment is denoted as M and reaction forces in the x and y directions as h and v, respectively. An arbitrary point $[\,x(\hat{u})\ \ y(\hat{u})\,]$ on the neutral axis is expressed as

$$x(\hat{u}) = x(0) + L\int_0^{\hat{u}} \cos\eta du\ ;\ \ y(\hat{u}) = y(0) + L\int_0^{\hat{u}} \sin\eta du\ , \tag{2}$$

where L is the beam length. For convenience, the un-deformed shapes of the four beams, when represented by the shape function η, is parameterized by using polynomials [17] as

$$\eta_i(u) = c_{i0} + c_{i1}u + \cdots + c_{im}u^m\ ;\ i = 1\text{–}4 \tag{3}$$

where coefficients c_{i0}–c_{im} decide the shape of the ith beam. The effect of the number of polynomial terms in Eq. (3) on the beam shape is depicted in Fig. 5. When only one term (c_0) presents, it corresponds to a straight beam with slope $\tan(c_0)$, as shown in Fig. 5(a). When considering both c_0 and c_1u, it describes an arc with

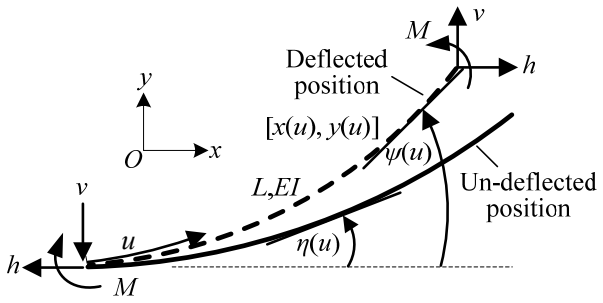

Fig. 4 Deformation model of a compliant beam

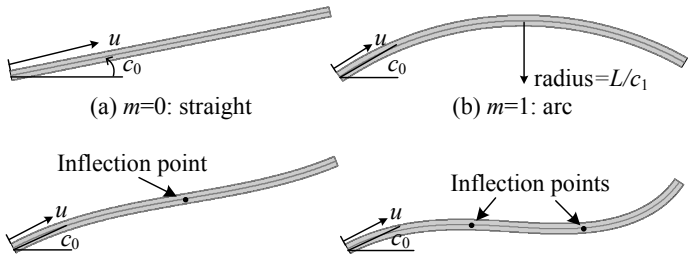

Fig. 5 Beam shapes using different number of polynomial terms

radius of curvature L/c_1, as shown in Fig. 5(b). When three terms present (m=2), it is a curve with at most one inflection point shown in Fig. 5(c). Similarly, a four-term polynomial has at most two inflection points shown in Fig. 5(d). Higher order polynomials can be further expected. The inflection points are the roots of $d\eta/du$=0. For an arbitrary combination of coefficients in Eq. (3), we have $[x' \; y'] = [L\cos\eta \;\; L\sin\eta] \neq 0$ for all $u \in [0\ 1]$, where a prime denotes derivative with respective to u. Thus beams represented by the shape functions are naturally free of cusps. This is beneficial compared to parameterizations based on Bezier or Hermite curves [16], as the prevention of cusps and near-cusp regions avoids stress concentration and manufacturing difficulties.

The governing equations of a deflected beam are extensively found in the literature (see Ref. [17] for an example). When a beam deflects, the bending moment and maximal bending stress are calculated as follows.

$$M = EI\frac{d(\psi-\eta)}{du};\ \sigma_m = \frac{Ew}{2L}\frac{d(\psi-\eta)}{du} \qquad (4, 5)$$

For slender beams, the axial and shear stresses are very small and are not considered, when compared to the bending stress. Since the beam shapes depend on the coefficients of the shape function in Eq. (3), they are formulated as design variables together with the three node positions ($\mathbf{n}_2$–$\mathbf{n}_4$). The number of design variables is 6+4(m+1) and it depends on the order of the shape functions. Aiming at making the force constant, formulation for the CFM shape design is detailed in Table 1.

There are four constraints in Table 1 to ensure convergence and that the converged optimal shape is feasible. Constraint (i) confines the dimension of the CFM by fixing the node positions on the design boundary. Constraint (ii) ensures that all the four beams stay within the rectangular boundary. To further prevent each beam from intersecting itself and with others, constraint (iii) limits the overall length of each link from exceeding a prescribed length. For constraint (iv), the maximal stress σ_m is calculated by using Eq. (5). It cannot exceed the allowable stress σ_y/SF, where σ_y is the yield stress and SF is the safety factor. Except for constraint (i), the other three are inequalities. The deformation analysis required in the optimization process is carried out by using the generalized (multiple) shooting method (GMSM) [17, 18]. This method is capable of accurate and efficient beam large deflection computation. The optimization is realized by using *fmincon*() in MATLAB®, where gradients are conveniently computed in a finite difference fashion.

Table 1 Formulation of CFM shape optimization

1. *Objective*: Given a Δ, minimize Eq. (1), which is a function of beam shapes and node positions.
2. *Design variables:* c_{i0}–c_{im} (i = 1–4), $\mathbf{n}_k = [n_{kx}\ n_{ky}]$ (k = 2–4)
3. *Constraints*:
(i) $\mathbf{n}_1$ = [0.25 0] cm; $\mathbf{n}_5$ = [0.25 4] cm; $\mathbf{n}_2$ has to lie on f_2.
(ii) The four curved beams (including $\mathbf{n}_3$ and $\mathbf{n}_4$) have to lie within the rectangular design boundary formed by functions f_1, f_2, f_3, and f_4.
(iii) The length of each beam cannot exceed a prescribed length. For convenience the prescribed length is 1.5 times the original straight beam (m=0) length.
(iv) The maximal stress σ_m within the beams cannot exceed the allowable stress σ_y/SF.

2.2 Optimal shape of the compliant constant-force mechanism

Based on the formulation in Table 1, we seek for the optimal shape and the corresponding relationship among the input displacement, reaction force, and maximal stress of a CFM. The simulation parameters are listed in Table 2. We use Polyoxymethylene as the material.

Table 2 Simulation parameters of the CFM

Δ=1.36cm	a = 0.88cm; b = 0.4cm
E = 2GPa (Young's modulus)	*SF* = 1.58; σ_y = 76 MPa (Yield stress)
w = 1mm (In-plane thickness)	t = 10mm (Out-of-plane thickness)
m = 2 (Order of shape function)	$[L_x\ L_y]$ = [3.2 4]cm (Design domain size); δ = 0.5cm

Fig. 6 shows the optimal original and deflected shapes of the CFM. Deformation primarily occurs in Beams 3 and 4 rather than Beams 1 and 2. A noticeable active inequality is constraint (ii) which limits the original shape of Beam 2 from exceeding boundary f_2. Another active inequality is constraint (iv), where the maximal stress (indicated in a circle between $\mathbf{n}_3$ and $\mathbf{n}_4$ in Fig. 6) equals to σ_y/SF. Fig. 7 shows the *F*–*Δ* and maximal stress curve, where F_d=9.736 N and c=0.7 cm. Hence the CFM needs a 0.7 cm preload in order to operate in the 0.66 cm constant-force range. The operational range of the optimized CFM is 48.5% of the entire displacement. The maximal stress curve and σ_y/SF line intersect at Δ=1.36 cm. Detailed numerical results are listed in Table 3.

In Eq. (1), only the flatness of the *F*–*Δ* curve is considered. Ideally it would be better to decrease the preload region in order to increase operational range. However, adding this mathematically into Eq. (1) would cause divergence. This is expectable since the *F*–*Δ* curve of typical elastic material is always continuous and cannot have a too sharp change of slope.

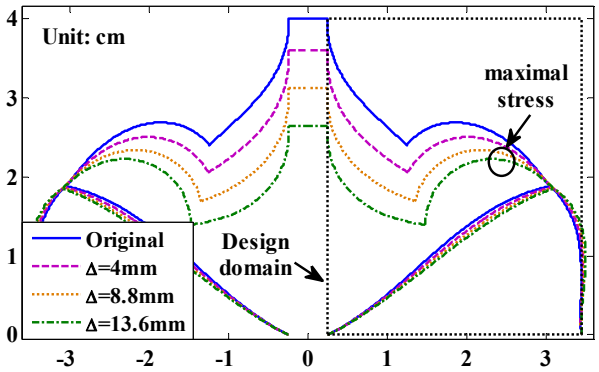

Fig. 6 Deflected shape (a=8.8mm and b=4mm)

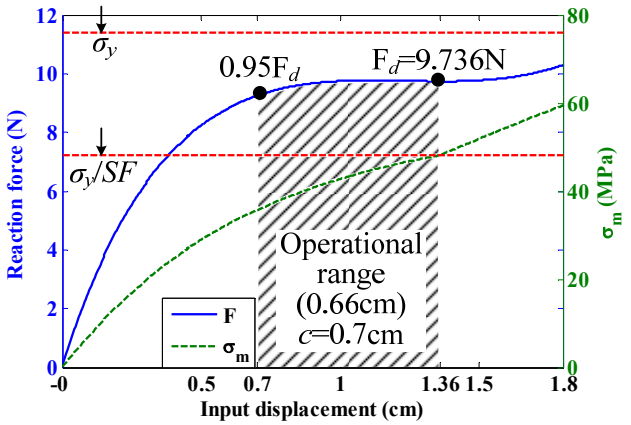

Fig. 7 Force to displacement curve (a=8.8mm and b=4mm)

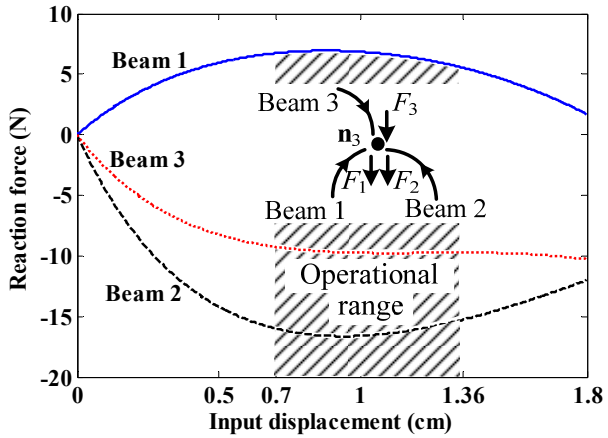

Fig. 8 Reaction force for each beam (in the vertical direction)

Table 3 Optimal configuration of the CFM

Position (cm)	Shape function (rad)	Length (cm)
$\mathbf{n}_1$=[0.25,0]	$\eta_1 = 0.4592 + 1.3092u - 1.5707u^2$	L_1 = 3.404
$\mathbf{n}_2$=[3.45, 0]	$\eta_2 = 1.6382 - 0.7560u + 1.5707u^2$	L_2 = 1.987
$\mathbf{n}_3$=[3.05, 1.877]	$\eta_3 = -4.081 + 0.3013u + 1.5707u^2$	L_3 = 2.199
$\mathbf{n}_4$=[1.244, 2.40]	$\eta_4 = 2.394 + 0.226u + 1.148u^2$	L_4 = 1.959

The reason for the constant output force may be explained by the interactions of beam reaction forces in the vertical direction. Fig. 8 shows the reaction forces of the three beams (denoted as v_1–v_3 for Beams 1–3) that connect at $\mathbf{n}_3$. In the operational range, the reaction force of Beam 3 remains nearly constant. On the other hand, both Beam 1 and Beam 2 exhibit an increase and decrease of reaction forces. Hence, Beams 1 and 2 take turns serving as the positive and negative stiffness mechanisms. The changes of the three forces roughly cancel with each other, resulting in a nearly constant force. Compared to CFMs where positive and negative stiffness mechanisms do not switch roles (see Fig. 1(b) for an example), the proposed CFM has a larger constant-force range.

2.3 Invariance of the F–Δ curve

When using the non-dimensional shape functions in Table 3 to describe the CFM, the form of the F–Δ curve is invariant provided the ratio L_x/L_y is unchanged. The CFM flexural rigidity and size can be adjusted to manipulate the magnitude (F_d) of the F–Δ curve without changing the constant-force proportion. This offers two advantages such that the optimized CFM is applicable to various situations without redoing another optimization. First, the nominal constant force F_d can be adjusted to a specified value by using the following formula:

$$F_{d1}L_{x1}^2/EI_1 = F_{d2}L_{x2}^2/EI_2 \quad (6)$$

where subscripts 1 and 2 denote the original and adjusted parameters, respectively. To obtain a specified nominal constant force F_{d2} from the original CFM, the values of EI_2 and L_{x2} must be changed to match with the specified F_{d2}. Among them, the size L_{x2} is adjusted by dimensionally scaling the CFM. The flexural rigidity EI_2 is adjusted by varying the in-plane thickness w, out-of-plane thickness t, or material. Note that changing in-plane thickness would as well change the maximal stress curve; changing material would change the yield and allowable stress. These in return alter the allowable input displacement.

Second, there is a range beyond Δ=13.6 mm in Fig. 7 that is nearly constant. However, a displacement beyond Δ=13.6 mm would violate the allowable stress (σ_y/SF). Without changing the F–Δ curve, we may move the maximal stress curve downward so that under the same allowable stress, the CFM has a larger operational range. According to Eq. (5), the maximal stress σ_m may be reduced by reducing the in-plane thickness w. To keep the flexural rigidity and thus F–Δ curve unaffected, the out-of-plane thickness t must be increased. As an illustration, the in-plane thickness w is multiplied by 0.85. The out-of-plane thickness t must be multiplied by 1.628 to produce the same I (I=tw^3/12). Fig. 9 shows the CFM with w=0.85 mm and t=16.28 mm. The F–Δ curve is the same as that in Fig. 7, except that the stress curve drops 8.92 MPa vertically. To satisfy the allowable stress, the force F_d now occurs at Δ=1.68 cm with preload c=0.788cm. This adjustment widens the operational range from 0.66 cm to 0.896 cm. This is more than 53% of the entire displacement.

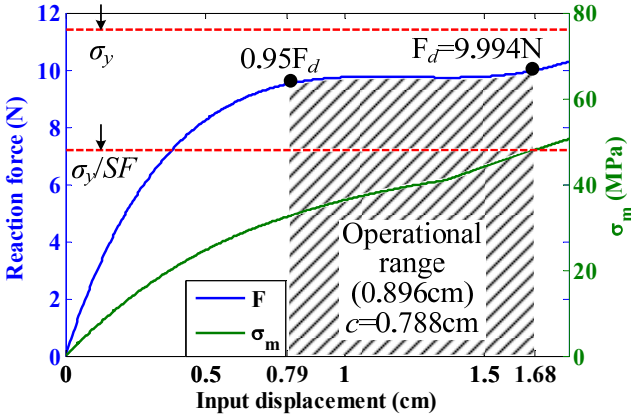

Fig. 9 Optimal result with the same flexural rigidity as Fig. 7

III. Experiment Validation

The results in Sec. 2 are validated by performing an experiment to obtain the actual F–Δ curve. Fig. 10 shows the experimental setup and CFM prototype. The CFM is fabricated by using the parameters in Tables 2–3, except that the in-plane thickness is reduced to $w = 0.85$ mm. We use a motorized stage to provide the linear input displacement. The reaction force at $\mathbf{n}_1$ is measured by a load cell from FUTEK (LSB200, maximum 22.27N, 0.01 N resolution). The CFM is given a Δ=1.6 cm displacement. Fig. 11(a) shows the experiment curve compared with those obtained by ANSYS® and the generalized multiple shooting method (GMSM). Three remarks are made by observing Fig. 11(a):

1. The GMSM curve agrees well with the ANSYS curve (BEAM3). This verifies our computation methods. However, neither curve matches with the experimental curve. The experimental reaction force is 0.9 N higher in the constant-force range than those predicted by simulations. The primary reason is that both the GMSM and BEAM3 element (in ANSYS) model beams as representative neutral axes. They fail to consider the effect of overlapping beam thicknesses at the connecting nodes. Fig. 11(b) illustrates the thickness effect at $\mathbf{n}_3$. The effective flexural rigidity of each beam near $\mathbf{n}_3$ becomes higher. Besides, there are unavoidable corner fillets (see Figs. 11(b–c)) due to the cutting tool diameter. This further increases the flexural rigidity. The corner fillets in Fig. 10(b) are created by using a cutting tool with 1 mm diameter.

2. To take the true geometry at the nodes into account, we simulate again by using SOLID186 element in ANSYS®. The CFM geometry with and without corner fillets (at $\mathbf{n}_1$ and $\mathbf{n}_3$) are both analyzed, as shown in Fig. 11(a). Compared with the GMSM and BEAM3 curves, the two SOLID186 curves match better with the experiment curve, while the effect of corner fillets is less obvious. The negligible difference between SOLID186 curves and experiment may be caused by machining error, especially in the out-of-plane direction (cutting depth).

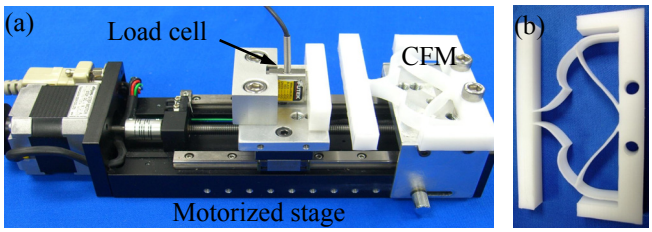

Fig. 10 Experiment setup and CFM prototype

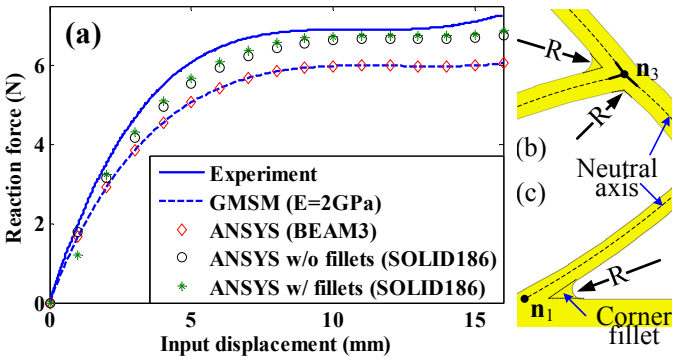

Fig. 11 (a) Experiment and simulation F–Δ curves
(b) Close view of $\mathbf{n}_3$ geometry (c) Close view of $\mathbf{n}_1$ geometry

3. Although the experimental F–Δ curve has a slightly larger constant force than that predicted by the four simulation curves in Fig. 11(a), the constant-force ranges show very much resemblance. This implies that the constant-force range of the CFM is insensitive to fabrication and modeling imperfections. In practice, the magnitude of constant force can be adjusted by the technique mentioned in Sec. 2.3.

IV. An Illustrative Application

Based on the previous design and analysis, a CFM is illustrated here for adaptive force regulation of robotic end-effectors. End-effectors may be subjected to external forces in the lateral and axial directions. For brevity, we consider an end-effector the axial force of which is of primary importance when interacting with the environment. To emulate a linearly moving end-effector along an unknown surface, we set up an experiment together with its CAD model in Fig. 12. The end-effector has an extruded triangular tip. The tip, when in practice, can be performing a cutting, welding, or deburring job. A CFM connects to the end-effector. To avoid unwanted bending deflections caused by tip lateral forces, two linear bearings are used to constrain the motion in the axial direction. One force sensor is connected serially to the CFM to measure the axial contact force introduced by the environment. The end-effector, CFM, and load cell are together carried by a motorized stage that moves linearly against a cam. The cam emulates an unknown environment. When the end-effector moves against the cam, it moves backward and squeezes the CFM due to increasing cam height.

To increase the structural stability, the CFM in Fig. 12 consists of two identical sub-CFMs. The CAD model of the sub-CFM is shown in Fig. 13. The in-plane and out-of-plane thicknesses are w = 0.4 mm and t = 6 mm. Each leg of the sub-CFM is enclosed by a 1×1cm design boundary. Its shape has been optimally designed by using a similar formulation as that in Table 1. Different from the CFM in Fig. 6, there is only one beam connecting to the ground, in order to extend the operational range. Table 4 shows the detailed CFM configuration.

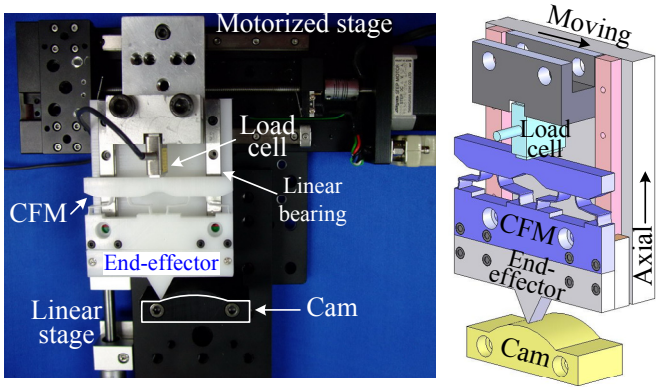

Fig. 12 Experiment setup and its CAD model

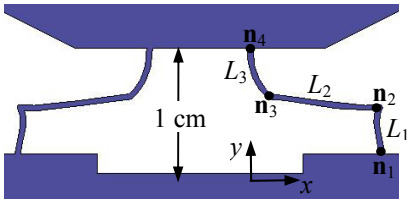

Fig. 13 CAD model of the sub-CFM

Table 4 Optimal configuration of the CFM

Position (cm)	Shape function (rad)	Length (cm)
$\mathbf{n}_1$=[1,0.2]	$\eta_1 = 1.6401 + 0.9920u - 1.5706u^2$	$L_1 = 0.360$
$\mathbf{n}_2$=[0.99,0.55]	$\eta_2 = 3.2380 - 0.8791u + 0.7358u^2$	$L_2 = 0.849$
$\mathbf{n}_3$=[0.15, 0.64]	$\eta_3 = 2.4429 - 1.1268u + 0.2199u^2$	$L_3 = 0.407$
$\mathbf{n}_4$=[0, 1]		

As the end-effector moves along the cam, its tip axial reaction force is recorded by a data acquisition card. Fig. 14 shows the reaction force curve when the end-effector tip moves along the cam profile with height gradually increasing up to 5 mm. The maximal reaction force is 8.59 N when the end-effector tip is at the top of the cam. The overall reaction force stays within 8 N to 8.59 N for the 12.3 mm transverse displacement. The end-effector moves at speed 0.25 mm/sec. Note that without a CFM, an extra actuator is required to raise the tip to prevent jam. This may bring in a controller to regulate the contact force, not to mention the overshoot and stability problems introduced by active control. On the other hand, our proposed CFM only requires a passive mechanism to adapt to the environment.

An important issue of a CFM is the constant-force range. For a single layer CFM shown in Fig. 12, the range of motion is primarily compromised by the maximal allowable stress. It can be increased by using two layers of the CFM shown in Fig. 15(a). The CFM can also be made circular to adapt to various geometry and application of the end-effector. One such prototype is shown in Fig. 15(b).

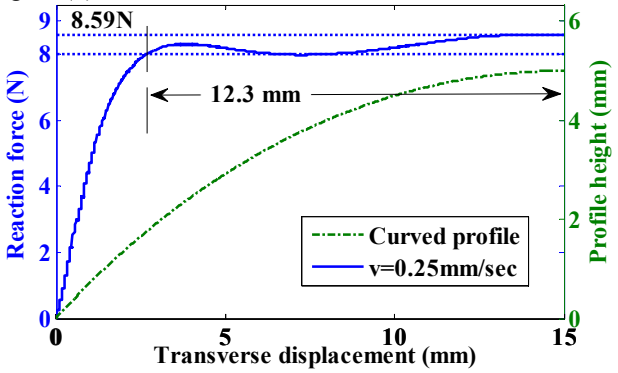

Fig. 14 Force profile with respect to trajectory

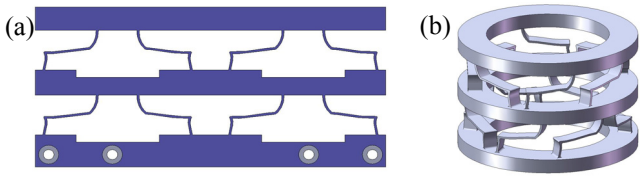

Fig. 15 Two-layer CFMs for increased range of motion

V. Conclusions

This paper presents the design and demonstration of a compliant constant-force mechanism (CFM). Compared to CFMs found in the literature, the proposed CFM composes of thin beams forming a monolithic piece. Hence it is free of wear and miniaturizable. Based on the developed optimization technique, the force to displacement curve exhibits a range that is as constant force as possible. The operational range is more than 50% of the entire displacement. The optimized CFM has been verified by simulation and experiment. Due to the invariance of the force to displacement curve, the CFM shape is generic and can be resized to fit with various situations. Under the same allowable stress, the operational range may be increased by adjusting the in-plane and out-of-plane thicknesses while its flexural rigidity is retained.

Finally, we illustrate the CFM for regulating robot end-effector contact force. When moving along a surface, the end-effector can adapt to a height variance of 5 mm while maintaining a nearly constant axial contact force (from 8 to 8.59 N). Two or more layers of CFMs may be assembled to increase the adaptation capability. Our future work will carry out a CFM design that provides constant forces in both the axial and lateral directions. We expect the proposed CFM can serve as an alternative to regulate end-effector forces in unknown and changing environments.

References

[1] http://www.vulcanspring.com/

[2] http://www.ati-ia.com/

[3] Sönmez, Ü., 2007, "*Introduction to Compliant Long Dwell Mechanism Designs Using Buckling Beams and Arcs*," J. Mech. Des., 129(8), 831.

[4] Nathan, R. H., 1985, "*A Constant Force Generation Mechanism*," ASME J. Mech., Transm., Autom. Des., 107, pp. 508-512.

[5] Weight, B.L., 2001, "*Development and Design of Constant-force Mechanisms*," Master's thesis, Department of Mechanical Engineering, Brigham Young University, Provo, UT.

[6] Boyle, C., Howell, L.L., Magleby, S.P., Evans, M.S., 2003, "*Dynamic Modeling of Compliant Constant-force Compression Mechanisms*," Mech. Mach. Theory **38**, 1469–1487.

[7] Nahar, D. and Sugar, T. G., 2003, "*Compliant Constant-Force Mechanism with a Variable Output for Micro/Macro Applications*," IEEE ICRA, Taipei, Taiwan.

[8] Pedersen, C. B. W., Fleck, N. A., Ananthasuresh, G. K., 2006, "*Design of a Compliant Mechanism to Modify an Actuator Characteristic to Deliver a Constant Output Force,*" ASME J. Mech. Des., **128**(5), pp. 1101-1112.

[9] Alabuzhev, P., Gritchin, A., Kim, L., Migirenko, G., Chon, V., and Stepanov, P., 1989, *Vibration Protecting and Measuring Systems with Quasi-Zero Stiffness*, Hemisphere Publishing, New York.

[10] Jenuwine, J. G., and Midha, A., 1994, "*Synthesis of Single-Input and Multiple-Output Port Mechanisms with Springs for Specified Energy Absorption*," ASME J. Mech. Des., **116**(3), pp. 937-943.

[11] Meaders, J. C. and Mattson, C. A., 2009, "*Optimization of Near-constant Force Springs subject to Mating Uncertainty*," Struct. Multidisc. Optim.

[12] Howell, L. L. and Magleby, S. P., 2006, "*Substantially Constant-force Exercise Machine*," US Patent, 7060012, B2.

[13] Igor Berliant, 2009, "Constant Force Rail Clamp," US Patent.

[14] Jung, S., Hsia, T. C., and Bonitz, R. G., 2004, "*Force Tracking Impedance Control of Robot Manipulators under Unknown Environment*," IEEE Trans. Control Syst. Technol., **12**(3), pp. 474–483.

[15] Mallapragada, V., Erol, D., and Sarkar, N., 2007, "*A New Method of Force Control for Unknown Environments*," Int. J. Adv. Robot. Syst., **4**(3), pp. 313-322.

[16] Salomon, D., 2006, *Curves and Surfaces for Computer Graphics*, Springer.

[17] Lan, C.-C., Lee, K.-M., 2006, "*Generalized Shooting Method for Analyzing Compliant Mechanisms with Curved Members*," ASME J. Mech. Des., **128**(4), pp. 765-775.

[18] Lan, C.-C. and Cheng, Y.-J., 2008, "*Distributed Shape Optimization of Compliant Mechanisms Using Intrinsic Functions*," ASME J. Mech. Des., **130**, 072304.